Modeling and Characterization of the Passive Bending Stiffness of Nanoparticle-Coated Sperm Cells using Magnetic Excitation

João M. S. Dias, Daniel Estima, Harmen Punte, Anke Klingner, Lino Marques, Veronika Magdanz, and Islam S. M. Khalil*

Of all the various locomotion strategies in low-*Re*, traveling-wave propulsion methods with an elastic tail are preferred because they can be developed using simple designs and fabrication procedures. The only intrinsic property of the elastic tail that governs the form and rate of wave propagation along its length is the bending stiffness. Such traveling wave motion is performed by spermatozoa, which possess a tail that is characterized by intrinsic variable stiffness along its length. In this paper, the passive bending stiffness of the magnetic nanoparticle-coated flagella of bull sperm cells is measured using a contactless electromagnetic-based excitation method. Numerical elasto-hydrodynamic models are first developed to predict the magnetic excitation and relaxation of nanoparticle-coated nonuniform flagella. Then solutions are provided for various groups of nonuniform flagella with disparate nanoparticle coatings that relate their bending stiffness to their decay rate after the magnetic field is removed and the flagellum restores its original configuration. The numerical models are verified experimentally, and capture the effect of the nanoparticle coating on the bending stiffness. It is also shown that electrostatic self-assembly enables arbitrarily magnetizable cellular segments with variable stiffness along the flagellum. The bending stiffness is found to depend on the number and location of the magnetized cellular segments.

1. Introduction

Soft microrobots hold prospects in various biomedical applications through their potential to perform noninvasive operations using gentle interactions with the surrounding tissue while maintaining a high level of control and propulsion efficiency.[1–4] The small size and excellent dexterity of these microrobots are promising features for delivery of a chemical agent to a target region with a higher degree of precision compared to conventional types of medicine,[5–8] thus, decreasing the negative side-effects in the rest of the healthy regions. In particular, biohybrid microrobots, consisting of artificial and biological components, have been developed as a special type of soft microrobots for selected applications such as active targeted drug delivery,[9] sensing,[10] and manipulation,[11] In this case, the biological component can act as a propulsion mechanism, an on-board energy source, a drug carrier, and a structural component.[12] These biological components are typically complemented by artificial structures which provide additional features, such as predictable response to external stimuli and the ability to emit detectable signals by noninvasive imaging systems. In order to fabricate such soft biohybrid microrobots, various flagellated cells (spermatozoa, bacteria, and algae) that serve as propulsion mechanisms have been assembled with synthetic microstructures.[13–15]

Another proposed method to fabricate magnetic microrobots takes a hybrid approach that combines nonmotile biological

J. M. S. Dias, D. Estima, H. Punte, I. S. M. Khalil
Department of Biomechanical Engineering
University of Twente
Enschede 7522 NB, The Netherlands
E-mail: i.s.m.khalil@utwente.nl

J. M. S. Dias, L. Marques
Institute of Systems and Robotics
University of Coimbra
Coimbra 3030-194, Portugal

A. Klingner
Department of Physics
The German University in Cairo
Cairo 11835, Egypt

V. Magdanz
Institute of Bioengineering of Catalonia
Smart Nanobiodevices group
Barcelona 08028, Spain

**ADVANCED
SCIENCE NEWS**

www.advancedsciencenews.com

**ADVANCED
THEORY AND
SIMULATIONS**

www.advtheorysimul.com

component to an artificial microstructure. Biotemplating has been performed previously based on the combination of plant or algae structures with synthetic magnetic elements.[16–18] This fabrication route has delivered rigid magnetic helical or needle-shaped microrobots, which move under the influence of a rotating magnetic field. Besides the plant structures, the organic bodies of some microorganisms and cells offer flexible templates for magnetic microswimmers when self-assembled with magnetic particles.[19,20] This approach utilizes the intrinsic flexibility of the sperm flagellum which varies along its length to create a swimmer with efficient locomotion under the influence of a dynamic magnetic field. A time-varying magnetic field can be used to actuate the sperm flagellum and propel the cell regardless of its lifetime.[19,20] The motion characteristics of a magnetically actuated passive flagellum differ from that of a live cell in that passively propagating waves initiated from a boundary cannot resemble those observed on an active flagellum with distributed contractile elements.[21] In addition, some cellular segments of the magnetically actuated passive flagellum are coated with nanoparticles, leading to significantly different mechanical properties from that of active flagella. Hence, the location of the magnetic segment along the cell is of importance for the locomotion in low Reynolds numbers (*Re*).[20] Alternative approaches to develop flexible microrobots have introduced magnetized elements in a desired design. For example, 3D magnetization profiles allow several designs to have complex modes of locomotion and shape changes.[22–24] In addition to the magnetization profile along the structure, the importance of intrinsic variable flexibility has also been proposed to obtain a desired shape.[25]

The compliance provided by the biological component is essential to break the time-reversal symmetry in low-*Re* flow, and can be used for flexible motion and gentle interaction with other cells and tissue. The bending stiffness along the length of the flagellum is an important parameter to enable correct theoretical predictions and simulations of sperm motion. The hydrodynamic interactions in low-*Re* are governed by the elastic properties of the swimmer, the rheological properties of the viscous medium, and the frequency of time-periodic deformations. These conditions define the pattern of the transverse waves that propagate along the soft body. In particular, the mean flagellar curvature of the flagellar beat is directly proportional to the curvature of the swimming path of the cell.[26] Thus, a detailed study of the mechanical properties of the sperm-templated microrobot is essential to provide maximum drag-based propulsive force.

In order to study the motility forces and bending stiffness of motile flagella and cilia, optical tweezers have been previously used.[27–29] The force generated by the optical trap was correlated to any other forces acting on the cell at the point of escape from the laser beam. This way the motility force of the spermatozoon was related to the threshold trapping power of the laser.[28] In a similar manner, Harada et al. have determined the bending stiffness of primary cilia of the renal epithelium.[30] To achieve controlled deformation, antibody-coated microspheres were attached to the tips of primary cilia and trapped by the laser. The trapping force was then correlated to the laser power, and the distance of the displacement at which the microspheres escape from

the laser was measured and correlated to the Young's modulus. Similarly, Xu et al. have studied the bending and shear stiffness of *Chlamydomonas* cilia using bends and counterbends.[31] Hill et al. have used magnetic beads to examine the force produced by cilia or flagella against an external load and estimated the axoneme stiffness.[32] They have demonstrated that the direction of the distal force does not influence the estimated bending stiffness. Lindemann et al. have measured the stiffness of impaled bull sperm flagella by bending the tail with a microprobe and measuring the relaxation time of the tail after release.[33]
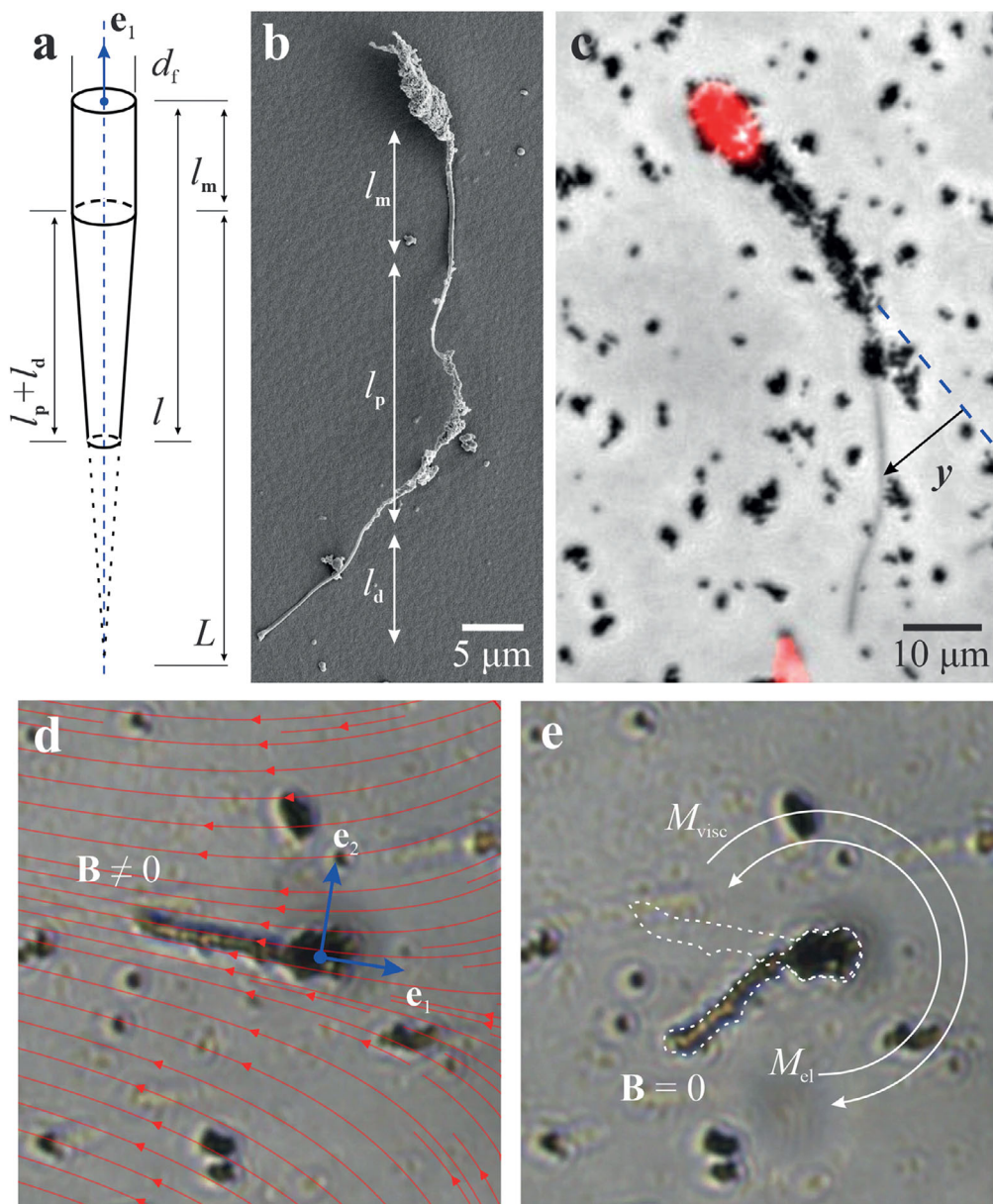
Details of the elasto-hydrodynamic interactions and wave propagation of sperm cells are not yet fully understood due to the lack of characterization of critical mechanical properties such as the internal resistive forces of the tail.[31] One of the unique properties of sperm cells is that their tail has a nonuniform bending stiffness along the length. This characteristic results in the typical waveform that is described by faster rate of propagation of waves near the distal end. In practice, measuring the exact bending stiffness of flagella is difficult in terms of implementation, cell handling, and repeatability. This difficulty arises from the fact that the implementation relies on excitation of a soft organic body at the microscale and relating a measurable response to desirable mechanical properties, and previous work have been limited to study the immutable elasticity of flagellar compounds. The vast majority of the previously mentioned studies have focused on live sperm cells and although these approaches are important in the determination of the bending stiffness, the properties of passive flagella and functionalized flagella must still be investigated. Developing methods for estimation of the bending stiffness is relatively challenging but will help understand how sperm cells perform their efficient swimming under different conditions.

Here, we take into account the impact of additional functionalities on the flagellum bending stiffness, such as magnetization and surface coating. Sperm-templated, self-assembled microrobots comprise a heterogeneity in terms of the particle distribution along their tail. This heterogeneity is particularly useful when designing and optimizing soft microrobots. In this study, we characterize the spatially varying bending stiffness due to the nonuniform magnetic nanoparticle coating along sperm flagella (**Figure 1**), and propose a wireless electromagnetic-based method to estimate the bending stiffness of such nonuniform flagella. Our method capitalizes on the transduction of magnetic energy into motion proportional to the stiffness of a passive flagellum surrounded by magnetizable nanoparticles. Energy is fed in by an external magnetic field and we measure decay rates of the flagellum to its initial configuration to determine the bending stiffness of flagella with disparate nanoparticle coatings.

2. Bending Stiffness of Particle-Coated Nonuniform Flagellum

2.1. Nanoparticle-Coated Soft Flagellum

Traveling-wave propulsion provides an effective method to swim through various viscous fluidic environments. If a filament of length l and bending stiffness $\kappa = IE$ deforms such that a

2100438 (2 of 15)

**ADVANCED
SCIENCE NEWS**

www.advancedsciencenews.com

**ADVANCED
THEORY AND
SIMULATIONS**

www.advtheorysimul.com

Figure 1. The bending stiffness varies along the flagellum due to a change in moment of area, $I(m, p, d; x)$, and elastic modulus, $E(m, p, d; x)$. a) It tapers gradually toward the distal end with a taper factor f. b) The location of the magnetizable cellular segment is determined during self-assembly and the indices m, p, d designate the magnetized region. c) The nanoparticles provide magnetization when magnetic field is applied yielding a deformation γ. d) The field, **B**, produces elastic deformation of the flagellum using magnetic torque exerted on its dipole moment. e) The elastic bending resistance of the passive flagellum is balanced by the viscous drag in the surrounding fluid when the field is removed, **B** = 0.
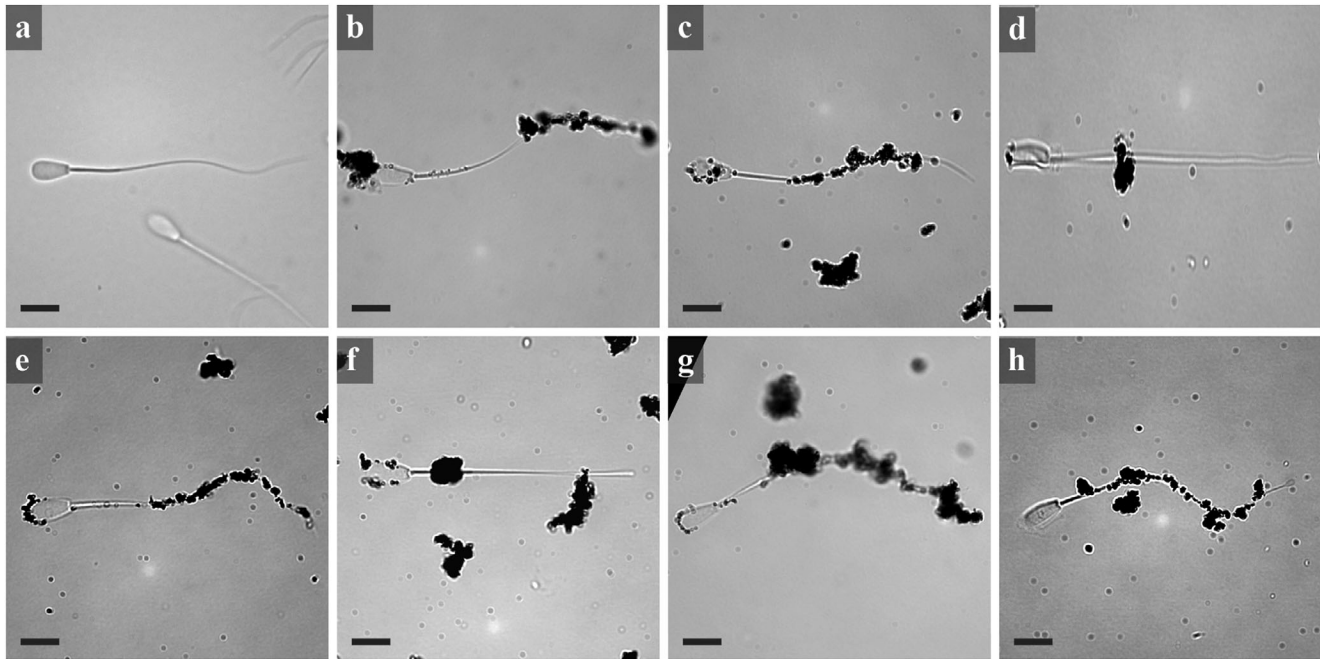
transverse bending wave is initiated at its proximal end to propagate toward its distal end, the steady-state solution of the balance of forces acting on any segment along the uniform filament will depend only on the sperm number[34]

$$\text{Sp} = l\left(\frac{\xi_\perp \omega}{\kappa}\right)^{1/4} \tag{1}$$

where $\xi_\perp$ is the normal drag coefficient, ω is the angular frequency, E is the modulus of elasticity, and I is the moment of area

of the cross-section. This is true only if the material has a uniform elastic modulus and cross-section along the length. In contrast, the flagellum displays remarkable complex internal structure, consisting of center and outer microtubles within a plasma membrane. It tapers gradually toward the distal end, as shown in Figure 1a,b). Therefore, the normal drag coefficient in Equation (1) varies along the length such that[35]

$$\xi_\perp(x) = \frac{4\pi\eta}{\log\left(l/D(x)\right) - 1} \tag{2}$$

2100438 (3 of 15)

**ADVANCED
SCIENCE NEWS**
www.advancedsciencenews.com

**ADVANCED
THEORY AND
SIMULATIONS**
www.advtheorysimul.com

Figure 2. Nanoparticles are assembled around the passive flagella of Bovine sperm cells (see Experimental Section) and result in spatially varying properties along the length. The dead cells are surrounded by elongated maghemite rice grain-shaped nanoparticles. Scale bar 10 µm. a) Fully uncoated. b) Distal-coated. c) Principal piece-coated. d) Midpiece-coated. e) Principal piece- and distal-coated. f) Midpiece- and distal-coated. g) Midpiece- and principal piece-coated. h) Fully coated.

where η is the viscosity of the medium and $D(x)$ is the diameter of the flagellum. The elastic modulus also depends on the location and concentration of the magnetizable nanoparticles. Figure 1c shows, for example, a passive midpiece-coated flagellum and under these conditions the elastic modulus will vary along the length based on the rule of mixture such that

$$E(m,p,d;x) = \begin{cases} E_s + \phi(E_p - E_s)m, & x \in \mathcal{L}_m \\ E_s + \phi(E_p - E_s)p, & x \in \mathcal{L}_p \\ E_s + \phi(E_p - E_s)d, & x \in \mathcal{L}_d \end{cases} \qquad (3)$$

where $E(m,p,d;x)$ is the elastic modulus of the nanoparticle-coated flagellum (see Experimental Section) and the combination (m,p,d) indicates the location of the magnetizable cellular segment, such that the midpiece-coated flagellum, principal piece-coated flagellum, and distal-coated flagellum with nanoparticles are designated by $m = 1$, $p = 1$, and $d = 1$, respectively, while the uncoated cellular segments are designated by $m = 0$, $p = 0$, and $d = 0$. In Equation (3), E_s and E_p are the modulus of elasticity of the organic body and the nanoparticles, respectively, and ϕ is a volume fraction between the organic body and the nanoparticles. Further, $\mathcal{L}_m = \{0 \le x \le l_m\}$, $\mathcal{L}_p = \{l_m \le x \le l_m + l_p\}$, and $\mathcal{L}_d = \{l_m + l_p \le x \le l\}$ are midpiece, principal piece, and distal end sets, respectively, where l_m is the length of the midpiece and l_p is the length of the principal piece.

Figure 2 shows eight representative nanoparticle-coated cells at different cellular segments. Each cellular segment can be made magnetic through nanoparticle-coating by surrounding the flagellum using electrostatic self-assembly (see Experi-

mental Section). Figure 2a shows a fully uncoated flagellum, whereas Figure 2b–d show distal-coated, principal piece-coated, and midpiece-coated flagella, respectively. The flagellum can also be coated at several cellular segments, as shown in Figure 2e for distal- and principal piece-coated flagellum, Figure 2f for midpiece- and distal-coated flagellum, and Figure 2g for midpiece- and principal piece-coated flagellum. Finally, Figure 2h shows a fully coated flagellum. Such flagellum exhibits spatially varying properties along the length based on the location of the nanoparticles.

We can also determine the influence of the nanoparticle coating on the diameter and moment of area of the flagellum based on the volume fraction, ϕ, between the organic body and the nanoparticles. If V_s and V_p denote the volumes of the organic body and nanoparticles, respectively, we have $\phi = V_p/(V_p + V_s)$ and it varies across the flagellum as follows

$$\phi(m,p,d;x) = \begin{cases} m\phi, & x \in \mathcal{L}_m \\ p\phi, & x \in \mathcal{L}_p \\ d\phi, & x \in \mathcal{L}_d \end{cases} \qquad (4)$$

Similarly, the volume fraction function describes the influence of the nanoparticle coating on the diameter of the filament which also varies across the length to affect the moment of area and Sp in Equation (1). To incorporate the effect of the nanoparticle coating into the moment of area, let us consider a segment of length Δx and diameter d_f along the nanoparticle-coated flagellum. If the volume of the organic component of this segment is $\Delta V_s = \pi d_f^2 \Delta x/4$, then the volume of the nanoparticle-coated

**ADVANCED
SCIENCE NEWS**

www.advancedsciencenews.com

**ADVANCED
THEORY AND
SIMULATIONS**

www.advtheorysimul.com

segment is $\Delta V = d_f^2 \Delta x \pi / (4(1 - \phi))$. Therefore, the diameter of the coated flagellum scales with the diameter of the uncoated flagellum as $\approx (1 - \phi)^{-0.5} d_f$, and we obtain

$$D(m, p, d; x) = \begin{cases} (1 - m\phi)^{-0.5} d_f, & x \in \mathcal{L}_m \\ (1 - p\phi)^{-0.5} d_f \left(1 - f\frac{x - l_m}{l_p + l_d}\right), & x \in \mathcal{L}_p \\ (1 - d\phi)^{-0.5} d_f \left(1 - f\frac{x - l_m}{l_p + l_d}\right), & x \in \mathcal{L}_d \end{cases} \quad (5)$$

where $f = (l_p + l_d) / L$ is the taper factor of the flagellum, l_d is the length of the distal end. Using Equation (5), the moment of area of the flagellum is calculated as

$$I(m, p, d; x) = \frac{\pi}{4} \left(\frac{D(m, p, d; x)}{2} \right)^4 \quad (6)$$

Therefore, the bending stiffness and the sperm number Sp (1) of the nanoparticle-coated flagellum are influenced by the volume fraction function $\phi(x)$ from Equations (2)–(6) for any actuation frequency ω, when a dynamic magnetic field is applied.

2.2. Magnetized Cellular Segments in a Magnetic Field

There is another effect of the nanoparticles on the dynamic response, since a distribution of bending moment $\mathcal{B}(m, p, d; x)$ is introduced when an external magnetic field, $\mathbf{B}$, is applied. The magnetic field magnetizes the nanoparticle clusters to magnetization $\mathbf{m}(m, p, d; x)$ that is directly proportional to the distribution of bending moment as $\mathcal{B}(m, p, d; x) = V_p \|\mathbf{m}(m, p, d; x) \times \mathbf{B}\|$. Following the same procedures as before, we can include the influence of the volume fraction function into the distribution of bending moment as follows:

$$\mathcal{B}(m, p, d; x) = \begin{cases} \frac{\pi}{4} \frac{m\phi\Delta x\|\mathbf{m}\|\|\mathbf{B}\|}{1 - m\phi} d_f^2, & x \in \mathcal{L}_m \\ \frac{\pi}{4} \frac{p\phi\Delta x\|\mathbf{m}\|\|\mathbf{B}\|}{1 - p\phi} d_f^2 \left(1 - f\frac{x - l_m}{l_p + l_d}\right)^2, & x \in \mathcal{L}_p \\ \frac{\pi}{4} \frac{d\phi\Delta x\|\mathbf{m}\|\|\mathbf{B}\|}{1 - d\phi} d_f^2 \left(1 - f\frac{x - l_m}{l_p + l_d}\right)^2, & x \in \mathcal{L}_d \end{cases} \quad (7)$$

Note that the distribution of bending moment includes maximum magnetic torque, $V_p \|\mathbf{m}(m, p, d; x)\| \|\mathbf{B}\|$, which implies that the flagellum will undergo maximum deformation, as shown in Figure 1d,e. Since the elastic (F_{el}) and magnetic (F_{mag}) force per unit length must equal the drag force per unit length (F_{visc}), the small deformation will be governed by the following force balance:

$$F_{el} + F_{mag} + F_{visc} = 0 \quad (8)$$

where the elastic force per unit length is given by

$$F_{el} = \frac{\partial^2}{\partial x^2} \left(\kappa(m, p, d; x) \frac{\partial^2 \gamma}{\partial x^2} \right) \quad (9)$$

where $\gamma(x, t)$ is the small amplitude and represents the deviation from the equilibrium position, and can be measured with respect to the material frame of reference of the sperm head $(\mathbf{e}_1, \mathbf{e}_2)$, as

shown in Figure 1c,d. The magnetic force per unit length depends on the distribution of bending moment (7), such that

$$F_{mag} = \frac{\partial^2 \mathcal{B}(m, p, d; x)}{\partial^2 x} \quad (10)$$

The viscous force is

$$F_{visc} = -\xi_\perp(x) \frac{\partial \gamma(x, t)}{\partial t} \quad (11)$$

In the case where the head is fixed to a solid boundary, both the amplitude, $\gamma(0, t)$, and its derivative with respect to x, $\partial \gamma(0, t) / \partial x$, are zero. Once an external magnetic field, $\mathbf{B}$, is applied, the nanoparticles are magnetized and the distribution of bending moment is introduced. Its contribution is indicated by the second term in the left-hand side of Equation (8). The total magnetic torque exerted on the magnetic dipole moment of the flagellum produces a deformation about the axis $\mathbf{e}_1 \times \mathbf{e}_2$, as shown in Figure 1d. Equations (2)–(8) complete the relation between the intrinsic variable stiffness due to the natural taper of the flagellum and the nonuniform nanoparticle coating along the length. Solving for flagellum deformation, we can predict the excitation and relaxation of the flagellum, for a given distribution of nanoparticle coating along the length and geometric parameters of the flagellum. If alternatively the flagellum is assumed to have a relatively small taper factor, then the presence of nonuniform nanoparticles coating leads to variable bending stiffness, resulting in a simplified models and analytical solution for the relaxation time.

2.3. Relaxation of a Nonuniform Flagellum

We turn to determine the relaxation based on the elastic force (9) which depends on varying bending stiffness along the length. We assume that the taper factor is relatively small ($f \approx 0$), and the bending stiffness is segment-wise constant $\kappa(x) = \kappa_m$ for $x \in \mathcal{L}_m$, $\kappa(x) = \kappa_p$ for $x \in \mathcal{L}_p$, and $\kappa(x) = \kappa_d$ for $x \in \mathcal{L}_d$, we have

$$\kappa(m, p, d; x) = \begin{cases} \kappa_m, & x \in \mathcal{L}_m \\ \kappa_p, & x \in \mathcal{L}_p \\ \kappa_d, & x \in \mathcal{L}_d \end{cases} \quad (12)$$

This bending stiffness can also be determined using the expressions of the rule of mixture (3) and moment of area (6). Assume that the decay time of the three magnetizable segments is the same, we have the following solution of the force balance (8)

$$\gamma(x, t) = w(m, p, d; x) e^{-t/\mathcal{T}(m, p, d)} \quad (13)$$

where $w(m, p, d; x)$ is the position dependent mode shape function and $\mathcal{T}(m, p, d)$ is the decay time of the flagellum to the initial configuration. We show in the next section that the decay time of any point along the length is approximately the same. In Equation (13), the mode shape of each cellular segment is given by

$$w(m, p, d; x) = \begin{cases} w_m(m, p, d; x), & x \in \mathcal{L}_m \\ w_p(m, p, d; x), & x \in \mathcal{L}_p \\ w_d(m, p, d; x), & x \in \mathcal{L}_d \end{cases} \quad (14)$$

Substituting Equation (13) for segment-wise constant bending stiffness into Equation (8) yields

$$\kappa(m, p, d; x) \frac{\mathrm{d}^4 w(m, p, d; x)}{\mathrm{d}x^4} = \frac{\xi_\perp(x)}{\mathcal{T}(m, p, d)} w(m, p, d; x). \tag{15}$$

Then it follows that the general solution of the mode shape of the magnetizable midpiece, w_m, is given by

$$w_\mathrm{m}(m, p, d; x) = A_\mathrm{1m}(m, p, d)e^{r_\mathrm{m}(m,p,d)x} +$$
$$A_\mathrm{2m}(m, p, d)e^{-r_\mathrm{m}(m,p,d)x} + A_\mathrm{3m}(m, p, d)\sin(r_\mathrm{m}(m, p, d)x) \tag{16}$$
$$+ A_\mathrm{4m}(m, p, d)\cos(r_\mathrm{m}(m, p, d)x)$$

where $r_\mathrm{m}(m, p, d)$ is a constant for the mode shape of the midpiece determined by the shape of the flagellum. The mode shape of the principal piece, w_p, is

$$w_\mathrm{p}(m, p, d; x) = A_\mathrm{1p}(m, p, d)e^{r_\mathrm{p}(m,p,d)x}$$
$$+ A_\mathrm{2p}(m, p, d)e^{-r_\mathrm{p}(m,p,d)x} + A_\mathrm{3p}(m, p, d)\sin(r_\mathrm{p}(m, p, d)x) \tag{17}$$
$$+ A_\mathrm{4p}(m, p, d)\cos(r_\mathrm{p}(m, p, d)x)$$

Similarly, $r_\mathrm{p}(m, p, d)$ is a constant for the mode shape of the principal piece determined by the shape of the flagellum. Finally, the mode shape of the distal end, w_d, is given by

$$w_\mathrm{d}(m, p, d; x) = A_\mathrm{1d}(m, p, d)e^{r_\mathrm{d}(m,p,d)x}$$
$$+ A_\mathrm{2d}(m, p, d)e^{-r_\mathrm{d}(m,p,d)x} + A_\mathrm{3d}(m, p, d)\sin(r_\mathrm{d}(m, p, d)x) \tag{18}$$
$$+ A_\mathrm{4d}(m, p, d)\cos(r_\mathrm{d}(m, p, d)x)$$

where $r_\mathrm{d}(m, p, d)$ is a constant for the mode shape of the distal. In Equations (16)–(18), $A_\mathrm{im}(m, p, d)$, $A_\mathrm{ip}(m, p, d)$, and $A_\mathrm{id}(m, p, d)$ are the ith constant depending on the conditions at the midpiece, principal piece, and distal end, respectively, for $i = 1, \ldots, 4$. Now using Equation (14) in Equation (15) we obtain

$$\mathcal{T}(m, p, d) = \frac{\xi_\perp(m, p, d)}{r_\mathrm{m}^4(m, p, d)\kappa_\mathrm{m}}$$
$$= \frac{\xi_\perp(m, p, d)}{r_\mathrm{p}^4(m, p, d)\kappa_\mathrm{p}} = \frac{\xi_\perp(m, p, d)}{r_\mathrm{d}^4(m, p, d)\kappa_\mathrm{d}} \tag{19}$$

Applying the boundary conditions at the two ends of the flagellum, we have

$$w(m, p, d; 0) = \frac{\mathrm{d}w(m, p, d; 0)}{\mathrm{d}x} = 0 \tag{20}$$

$$\frac{\mathrm{d}^2 w(m, p, d; l)}{\mathrm{d}x^2} = \frac{\mathrm{d}^3 w(m, p, d; l)}{\mathrm{d}x^3} = 0 \tag{21}$$

The connection between the midpiece and principal piece is continuous and smooth, such that

$$\frac{\mathrm{d}^i w_\mathrm{m}(m, p, d; l_\mathrm{m})}{\mathrm{d}x^i} = \frac{\mathrm{d}^i w_\mathrm{p}(m, p, d; l_\mathrm{m})}{\mathrm{d}x^i}$$
$$\text{for } i = 0, \ldots, 3 \tag{22}$$

Similarly, the connection between the principal piece and distal end is continuous, we have

$$\frac{\mathrm{d}^i w_\mathrm{p}(m, p, d; l_\mathrm{m} + l_\mathrm{p})}{\mathrm{d}x^i} = \frac{\mathrm{d}^i w_\mathrm{d}(m, p, d; l_\mathrm{m} + l_\mathrm{p})}{\mathrm{d}x^i}$$
$$\text{for } i = 0, \ldots, 3 \tag{23}$$

Now using the boundary conditions (20)–(23) we obtain the following system of algebraic homogenous equations

$$\mathcal{M}(r_\mathrm{m}(m, p, d))\mathcal{A} = 0 \tag{24}$$

where $\mathcal{M}$ is a coefficient matrix and $\mathcal{A}$ is a vector with the constants in Equations (16)–(18), such that
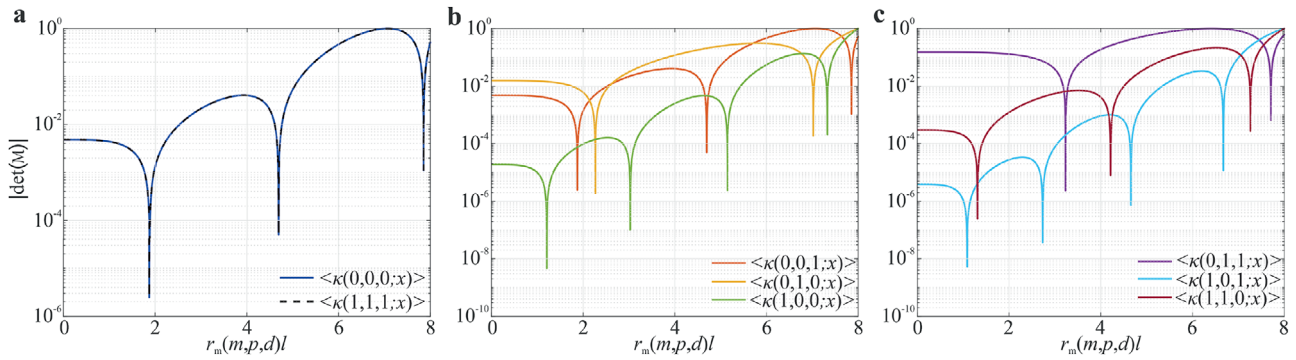
$$\mathcal{A} = \begin{bmatrix} A_\mathrm{1m} & \ldots & A_\mathrm{4m} & | & A_\mathrm{1p} & \ldots & A_\mathrm{4p} & | & A_\mathrm{1d} & \ldots & A_\mathrm{4d} \end{bmatrix}^T \tag{25}$$

Note that $\mathcal{M}$ is characterized by one of the constants $r_\mathrm{m}(m, p, d)$, $r_\mathrm{p}(m, p, d)$, or $r_\mathrm{d}(m, p, d)$ since they are related based on the decay time in Equation (19). **Figure 3** shows the absolute value of the determinant of $\mathcal{M}$ versus $r_\mathrm{m}(m, p, d)l$. For each type of magnetizable flagella, the local minima indicate nontrivial solutions of Equation (24). The first local minima at $r_\mathrm{m}(m, p, d)l$ is used together with Equations (19) to obtain the relaxation constant $\mathcal{T}$ for each group. The aim is to determine the bending stiffness for a given set of parameters for each group of nanoparticle-coated flagella. This is an alternative approach based on the parameters of the flagellum and can be used to directly determine the bending stiffness without simulating the dynamic response to determine the relaxation time. Alternatively, the relation between bending stiffness and $\mathcal{T}$ for homogenous tails derived by Rikmenspoel[36] can be extended and used based on numerical or experimental results. For groups with inhomogenous bending stiffness (κ depends on x), an apparent bending stiffness is defined as

$$\langle \kappa(m, p, d) \rangle = \left(\frac{l}{\mu} \right)^4 \frac{\xi_\perp}{\mathcal{T}(m, p, d)} \tag{26}$$

where $\mu = 1.875$ is the first mode of the characteristic equation of the force balance (8) when the magnetic field is removed. The operator $\langle \cdot \rangle$ denotes averaging over the length of the flagellum, and $\mathcal{T}(m, p, d)$ is its decay time to the initial configuration. This extended definition gives the same results for homogenous groups. Equation (26) is valid for all eight groups (Figure 2). It connects $\mathcal{T}$ with the apparent bending stiffness and by solving Equation (8), for a given set of parameters (ϕ, E_p, and E_s), we can directly determine the bending stiffness from the calculated or measured dynamic response of the flagellum after removal of the magnetic fields. Consider, for example, a fully uncoated and fully coated flagella of length $l = 60$ μm, the above expression (26) reduces to

$$\langle \kappa(0, 0, 0) \rangle = 1.05 \times 10^{-18} \frac{\xi_\perp(x)}{\mathcal{T}(0, 0, 0)}$$

$$\langle \kappa(1, 1, 1) \rangle = 1.05 \times 10^{-18} \frac{\xi_\perp(x)}{\mathcal{T}(1, 1, 1)} \tag{27}$$

**ADVANCED
SCIENCE NEWS**

www.advancedsciencenews.com

**ADVANCED
THEORY AND
SIMULATIONS**

www.advtheorysimul.com

Figure 3. The absolute values of the determinant of $\mathcal{M}$ are calculated versus $r_m(m, p, d)l$ for all groups. The minima of $|\mathcal{M}|$ indicate nontrivial solutions of Equation (24). a) For a fully uncoated and fully coated flagella, minimum $|\mathcal{M}|$ is found at $r_m(0, 0, 0)l = r_m(1, 1, 1)l = 1.875$. b) For distal-coated, principal piece-coated, and midpiece-coated flagella, minimum $|\mathcal{M}|$ is found at $r_m(0, 0, 1)l = 1.875$, $r_m(0, 1, 0)l = 2.266$, and $r_m(1, 0, 0)l = 1.209$, respectively. c) For flagella with two coated cellular segments, $r_m(0, 1, 1)l = 3.231$, $r_m(1, 0, 1)l = 1.086$, and $r_m(1, 1, 0)l = 1.3127$.

Note that the constant μ that minimizes $|\mathcal{M}|$ for fully coated and fully uncoated flagella is approximately the same. However, they differ in that each restores its original configuration at decay rate of $\mathcal{T}(0, 0, 0)$ and $\mathcal{T}(1, 1, 1)$, respectively. By repeating the same procedure for different groups of nanoparticle-coated flagella, the corresponding bending stiffness are extracted from measured or calculated $\mathcal{T}(m, p, d)$.

Combining Equations (19) and (26), the apparent bending stiffness can be calculated as

$$\langle \kappa(m, p, d) \rangle = (r_m(m, p, d)l/\mu)^4 \kappa_m \tag{28}$$

Then it is straightforward to determine the bending stiffness based on the constant $r_m(m, p, d)$ at which $|\mathcal{M}|$ is minimum (Figure 3). Consider, for example, distal-coated, principal piece-coated, and midpiece-coated flagella (Figure 2b), the values of $r_m(0, 0, 1)l$, $r_m(0, 1, 0)l$, and $r_m(1, 0, 0)l$ that minimize $|\mathcal{M}|$ are 1.875, 2.266, and 1.209, respectively. Again, the above expression (28) reduces to

$$\langle \kappa(0, 0, 1) \rangle = \kappa_m$$

$$\langle \kappa(0, 1, 0) \rangle = \left(\frac{2.266}{1.875} \right)^4 \kappa_m$$

$$\langle \kappa(1, 0, 0) \rangle = \left(\frac{1.209}{1.875} \right)^4 \kappa_m \tag{29}$$

This apparent bending stiffness found by calculation can then be compared to apparent bending stiffness found from numerical and experimental results based on Equation (26). The problem thus reduces to finding the decay time numerically or experimentally by magnetic excitation and relaxation of the magnetizable cells and from decay time with Equation (26). If alternatively the parameters are given, then Equation (28) can be used to estimate the bending stiffness.

3. Magnetic Excitation and Relaxation

Since the calculation of apparent bending stiffness in Equation (26) is only for a relatively small taper factor $f \approx 0$, the

force balance (8) and the boundary conditions are also solved numerically by finite difference method. If the proximal end of the nanoparticle-coated flagellum is constrained ($\gamma(0, t) = \partial\gamma(0, t)/\partial x = 0$), the free end will deform under the influence of external force or torque. When an external magnetic field is applied (see Experimental Section), the field magnetizes the cluster of nanoparticles to a magnetization $\mathbf{m}(m, p, d; x)$. Although there exist several magnetizable clusters along the flagellum, the local magnetic torques enable the flagellum to deform in the same direction about the axis $\mathbf{e}_1 \times \mathbf{e}_2$. In this case, the induced magnetization, $\mathbf{m}(m, p, d; x)$, of each cluster along the flagellum is enclosed between the local tangent along the length and the direction of the magnetic field, $\mathbf{B}$, and the contribution of the magnetic torque is introduced by the second term in Equation (8). The magnetic torque vanishes after the magnetic field is set to zero and in this case the relaxation of the flagellum is governed by balance between the elastic and drag forces only. Note that unlike the nanoparticle-coated flagellum, the uncoated flagellum is not influenced by the external magnetic field. Therefore, the uncoated flagellum of bending stiffness $\kappa(0, 0, 0; x)$ can be excited only by applying a contact force at the distal end.

3.1. Fully Uncoated and Coated Flagellum

The behavior of the uncoated and nanoparticle-coated flagella is shown in **Figure 4**. Computations are done using the balance of magnetic, elastic, and viscous drag forces using the abovementioned boundary conditions for magnetic excitation and relaxation. Figure 4a shows the time-dependent deformation of an uncoated flagellum of bending stiffness $\kappa(0, 0, 0; x)$. In this case, the elastic modulus is uniform ($E_s = 1.8$ MPa) and the bending stiffness varies along the length based on Equations (3) and (5) due to the natural taper of the flagellum toward the distal end ($f \approx 0.4$). Note also that the displacement field shown in Figure 1 is determined by imposing distal end force such that the maximum deformation of the distal end is 10% (≈ 6 µm) of the length of the flagellum.

Equations (3)–(5) are used to define the average bending stiffness over the length and the deformation and relaxation are calculated for $m = p = d = 0$, as shown in Figure 4a,b,
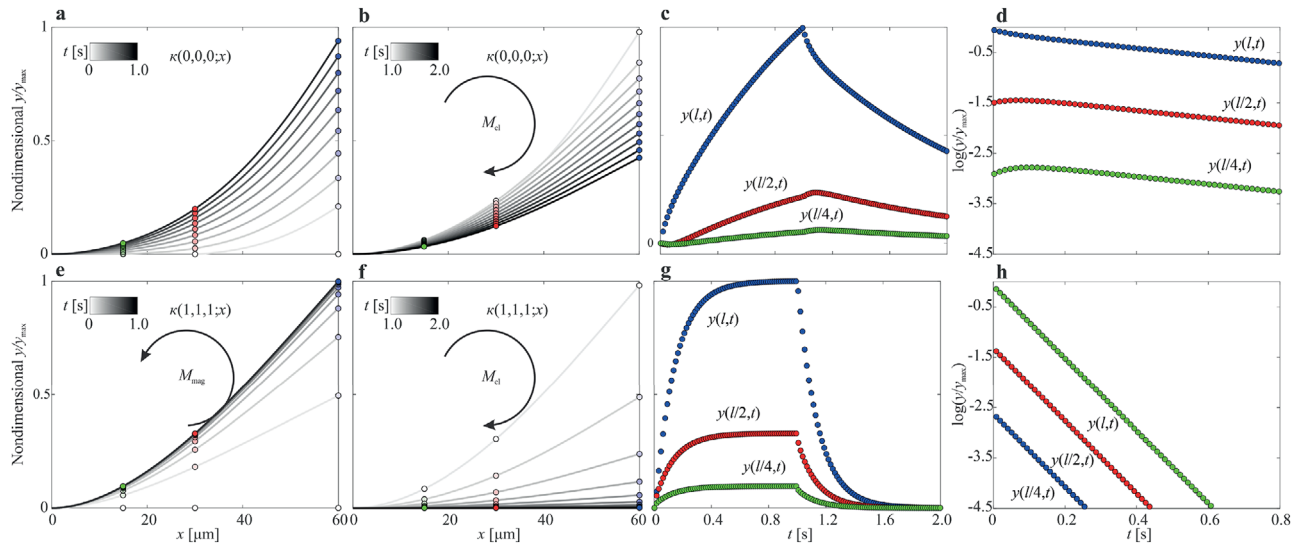
Figure 4. Simulation results of two flagella of bending stiffness $\langle\kappa(0,0,0)\rangle$ and $\langle\kappa(1,1,1)\rangle$. Parameters: $\eta = 1$ mPa.s, $l = 60$ µm, $d_f = 1$ µm, $l_m = 13$ µm, $l_p = 40$ µm, and $l_d = 7$ µm. Darker curves indicate later times. a–d) The passive flagellum is driven by distal contact force. The force is removed and the elastic moment restores its original shape. Position of the filament at l, $l/2$, and $l/4$ are calculated versus time and the decay time $\mathcal{T}$ is calculated from the slope of $\log(y)$. The average decay rate is $1/\mathcal{T}(0,0,0) = 0.7$ s^{-1}. e,h) The passive flagellum is driven by magnetic field and nanoparticle coating. Energy is fed in by a magnetic torque through a distribution $\mathcal{B}(1,1,1;x)$. The flagellum returns to its original shape when the applied field is removed. The decay rate is $1/\mathcal{T}(1,1,1) = 7.2$ s^{-1}.

respectively. The amplitude normalized by the maximum deformation (y/y_{max}) of three points at one-fourth and one-half of the length and at the tip are shown versus time in Figure 4c. Once a force is applied at the distal end, the amplitude of these three points (green, red and blue circles) increases almost linearly with time, and decreases at slower rates after the external force is removed. The points at one-fourth and one-half of the length restore their initial configuration at decay rates of 0.64 and 0.69 s^{-1}, respectively. The point at the tip of the flagellum restores its location at faster decay rate than any other point along the flagellum, at a rate of 0.77 s^{-1}, as shown in Figure 4d. Substituting the calculated relaxation time into Equation (26), the calculated bending stiffness is $\langle\kappa(0,0,0)\rangle = 4.73 \times 10^{-21}$ N m^2. Alternatively, Equation (28) gives bending stiffness of $\langle\kappa(0,0,0)\rangle = 4.61 \times 10^{-21}$ N m^2 based on the parameters of the fully uncoated flagellum (see Experimental Section).

In the case of nanoparticle-coated flagellum at all of its cellular segments, we have $m = p = d = 1$, and therefore the elastic modulus of the organic body E_s and elastic modulus of the nanoparticles E_p defines the intrinsic elastic modulus using Equations (3) and (4). Similarly, Equation (5) gives the diameter of the nanoparticle coated flagellum. The following magnetic field is applied with respect to the local frame of reference ($\mathbf{e}_1$, $\mathbf{e}_2$)

$$\mathbf{B} = \begin{cases} B_0 \begin{pmatrix} 0 & 1 & 0 \end{pmatrix}, & \text{excitation} \\ 0, & \text{relaxation} \end{cases} \tag{30}$$
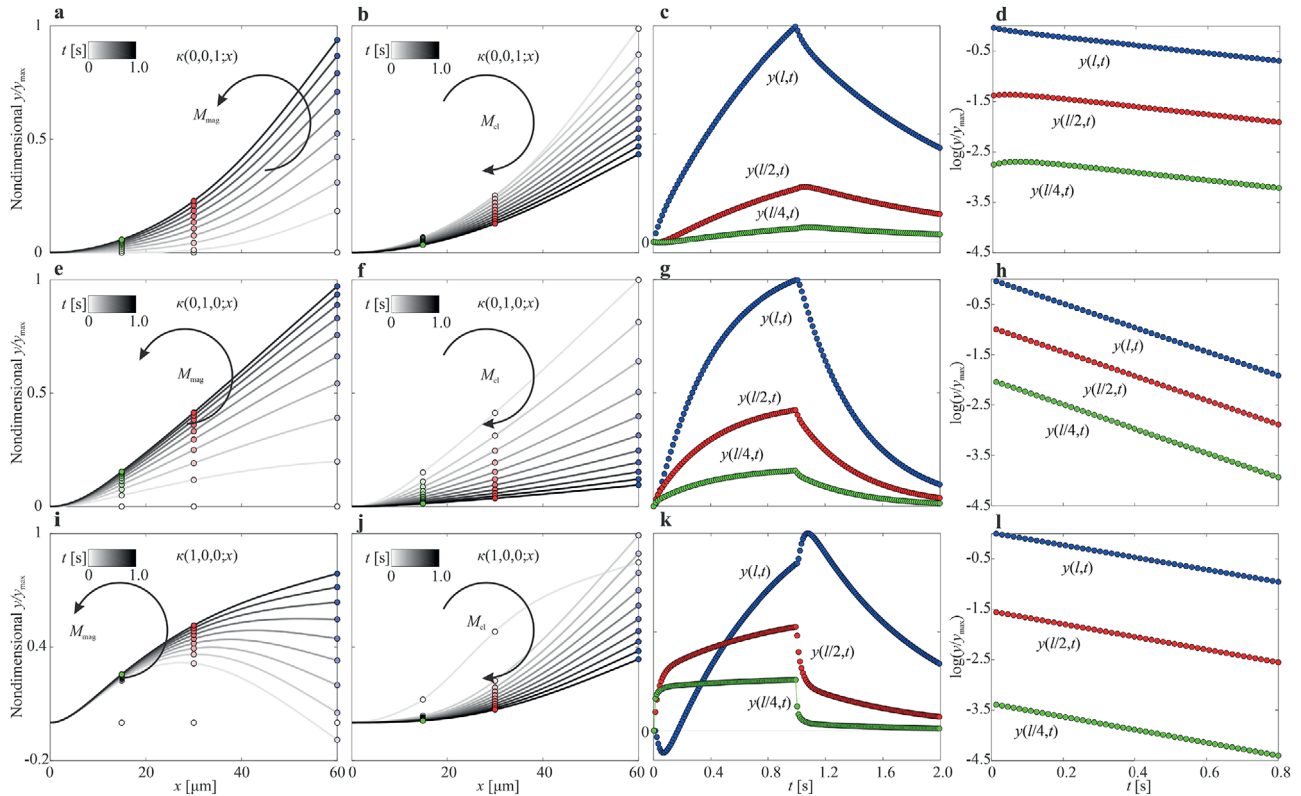
where B_0 is the magnitude of the magnetic field. The response of the nanoparticle-coated flagellum is shown in Figure 4e,f during magnetic excitation and relaxation, respectively. Note that unlike the uncoated flagellum case, the response and relaxation of the

three points are much faster when the flagellum is fully coated (Figure 4g). The points at one-fourth and one-half of the length restore their initial locations at decay rates of 7.17 and 7.21 s^{-1}, respectively, while the point at the tip has a decay rate of 7.22 s^{-1}, as shown in Figure 4h. Note also that unlike the uncoated flagellum, the decay rates of all points along the nanoparticle-coated flagellum are the same. The response is expected as the nanoparticle coating has a direct effect on the modulus of elasticity of the coated flagellum (3) and its moment of area (6), and since each cellular segment is coated, all points along the length restore their locations at the same decay rate. Using Equation (26) the bending stiffness is $\langle\kappa(1,1,1)\rangle = 16.38 \times 10^{-21}$ N m^2, whereas Equation (28) gives $\langle\kappa(1,1,1)\rangle = 16.08 \times 10^{-21}$ N m^2.

3.2. Single Magnetized Cellular Segment

In contrast to the previous cases where the flagellum is either fully uncoated or fully coated with nanoparticles, a flagellum with a single magnetized cellular segment is locally composed of an organic body and nanoparticles. When the distal end of the flagellum is coated only ($m = p = 0$ and $d = 1$), the three points at one-fourth and one-half of the length and at the tip have a relatively slow response similar to that of an uncoated flagellum, as shown in **Figure 5**a–c. The decay rate of these three points are 0.71, 0.74, and 0.78 s^{-1}, respectively (Figure 5d). Therefore, the response and relaxation of an uncoated flagellum is similar to that of a coated flagellum at the distal end. Using the calculated relaxation time, Equation (26) gives apparent bending stiffness of $\langle\kappa(0,0,1)\rangle = 6.54 \times 10^{-21}$ N m^2, while Equation (28) gives bending stiffness of $\langle\kappa(0,0,1)\rangle = 4.61 \times 10^{-21}$ N m^2 based on the parameters of the distal-coated flagellum.

**ADVANCED
SCIENCE NEWS**
www.advancedsciencenews.com

**ADVANCED
THEORY AND
SIMULATIONS**
www.advtheorysimul.com

Figure 5. Simulation results of distal-coated $\langle \kappa(0,0,1) \rangle$, principle piece-coated $\langle \kappa(0,1,0) \rangle$, and midpiece-coated $\langle \kappa(1,0,0) \rangle$ flagella. Parameters: $\eta = 1$ mPa.s, $l = 60$ μm, $d_f = 1$ μm, $l_m = 13$ μm, $l_p = 40$ μm, and $l_d = 7$ μm. Energy is fed in by a magnetic field (**B**) and a distribution of bending moment $\mathcal{B}(m, p, d; x)$. Position of the filament at l, $l/2$, and $l/4$ are calculated versus time and the decay time $\mathcal{T}$ is calculated from the slope of $\log(y)$. a–d) Energy is fed in by the distal-coated flagellum. The decay rate is $1/\mathcal{T}(0,0,1) = 0.74$ s^{-1}. e–h) Energy is fed in by the principle piece-coated flagellum and $1/\mathcal{T}(0,1,0) = 2.38$ s^{-1}. i–l) Energy is fed in by the midpiece-coated flagellum and $1/\mathcal{T}(0,0,1) = 1.25$ s^{-1}.
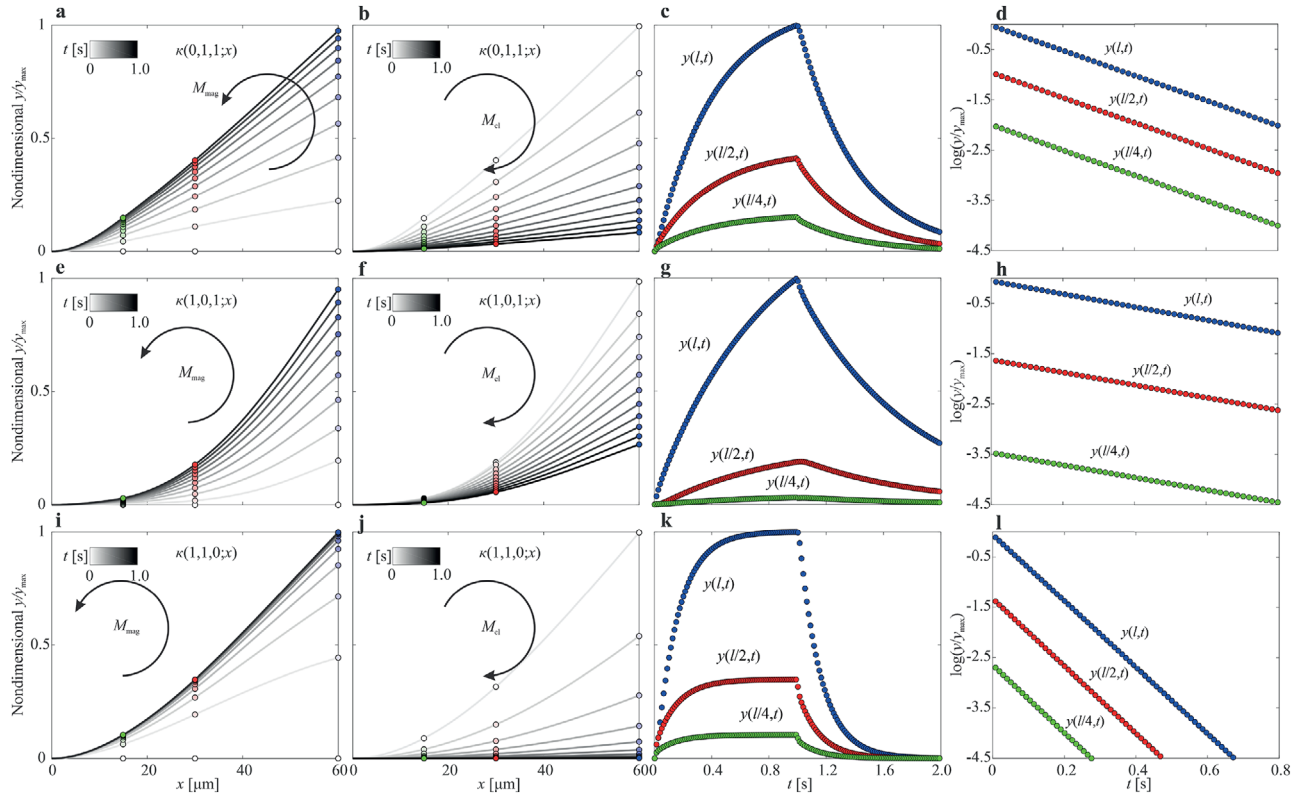
Figure 5e,f show the deformation and relaxation of a flagellum coated at its principal piece ($m = d = 0$ and $p = 1$). In this case the decay rates of the three points are 2.40, 2.39, and 2.37 s^{-1}, as shown in Figure 5g,h. Therefore, the relaxation of the coated flagellum at the principal piece is similar to that of a fully coated flagellum in that both have uniform decay rate regardless of the location of the observation point along the length. However, the decay rate decreases as the observation point approaches the distal end, unlike the increasing decay rate toward the distal end in the case of the fully coated flagellum. Using the average relaxation time of the principal piece-coated flagellum, the bending stiffness is $\langle \kappa(0,1,0) \rangle = 8.28 \times 10^{-21}$ and $\langle \kappa(0,1,0) \rangle = 8.06 \times 10^{-21}$ N m^2 using Equations (26) and (28), respectively.

Finally, when the midpiece is coated with nanoparticles only (($m = 1$ and $p = d = 0$)), the decay rates of the three observation points are calculated as 1.28, 1.26, and 1.21 s^{-1}, as shown in Figure 5i–l. The corresponding bending stiffness is calculated using Equation (26) as $\langle \kappa(1,0,0) \rangle = 4.72 \times 10^{-21}$ N m^2. The point at one-fourth of the length has a greater decay rate than any other point because it is the closest to the magnetized segment. Therefore, its response and decay rates are faster due to the location of the nanoparticles near to this point. Using Equation (28), the calculated bending stiffness based on the parameters of the midpiece-coated flagellum is $\langle \kappa(0,1,0) \rangle = 6.42 \times 10^{-21}$ N m^2.

3.3. Two Magnetized Cellular Segments

Now suppose we consider a flagellum coated at two cellular segments such that the head is fixed as before. In this case, the computations of the deformation and relaxation are done for flagella with bending stiffness of $\langle \kappa(0,1,1) \rangle$, $\langle \kappa(1,0,1) \rangle$, and $\langle \kappa(1,1,0) \rangle$. **Figure 6**a,b show the deformation and relaxation of a coated flagellum at the principal piece and the distal end ($m = 0$ and $p = d = 1$). The position of the three observation points with time indicates that the decay rates are 2.51, 2.50, and 2.48 s^{-1}, as shown in Figure 6c,d. The response and relaxation rates of nanoparticle-coated flagellum at the principle piece and distal end are similar to those observed for a flagellum coated at the principal piece, as shown in Figure 5h. The corresponding bending stiffness is $\langle \kappa(0,1,1) \rangle = 16.34 \times 10^{-21}$ N m^2, while Equation (28) gives $\langle \kappa(0,1,1) \rangle = 16.03 \times 10^{-21}$ N m^2 based on the nominal parameters.

When the midpiece and the distal end of the flagellum are coated (Figure 6e–h), the flagellum restores its original configuration at a slower rate compared to that of the coated flagellum at the principal and distal end ($1/\mathcal{T}(1,0,1) = 1.25$ s^{-1}), as shown in Figure 6g,h. The decay rate of the three observation points (from the $l/4$ to l) are 1.22, 1.24, and 1.28 s^{-1}, respectively. Again, we observe that the response and relaxation rates

**ADVANCED
SCIENCE NEWS**

www.advancedsciencenews.com

**ADVANCED
THEORY AND
SIMULATIONS**

www.advtheorysimul.com

Figure 6. Simulation results of principle piece- and distal-coated $\langle\kappa(1, 0, 1)\rangle$, midpiece- and distal-coated $\langle\kappa(1, 0, 1)\rangle$, and midpiece- and principle piece-coated $\langle\kappa(1, 1, 0)\rangle$ flagella. $\eta = 1$ mPa.s, $l = 60$ μm, $d_f = 1$ μm, $l_m = 13$ μm, $l_p = 40$ μm, and $l_d = 7$ μm. Energy is fed in by a magnetic field (**B**) and a distribution of bending moment $\mathcal{B}(m, p, d, x)$. Position of the filament at l, $l/2$, and $l/4$ are calculated versus time and the decay time $\mathcal{T}$ is calculated as the slope of $\log(y)$. a–d) The decay rate is $1/\mathcal{T}(0, 1, 1) = 2.5$ s^{-1}. e–h) The decay rate is $1/\mathcal{T}(1, 0, 1) = 1.25$ s^{-1}. i–l) The decay rate is $1/\mathcal{T}(1, 1, 0) = 6.6$ s^{-1}.

do not vary across the length as the number of magnetizable cellular segments increases. The corresponding bending stiffness of the midpiece- and distal-coated flagellum is $\langle\kappa(1, 0, 1)\rangle = 6.54 \times 10^{-21}$ N m^2. Alternatively, setting $m = d = 1$ and $p = 0$ and using Equations (3)–(6) and (28) the bending stiffness is $\langle\kappa(1, 0, 1)\rangle = 4.64 \times 10^{-21}$ N m^2.
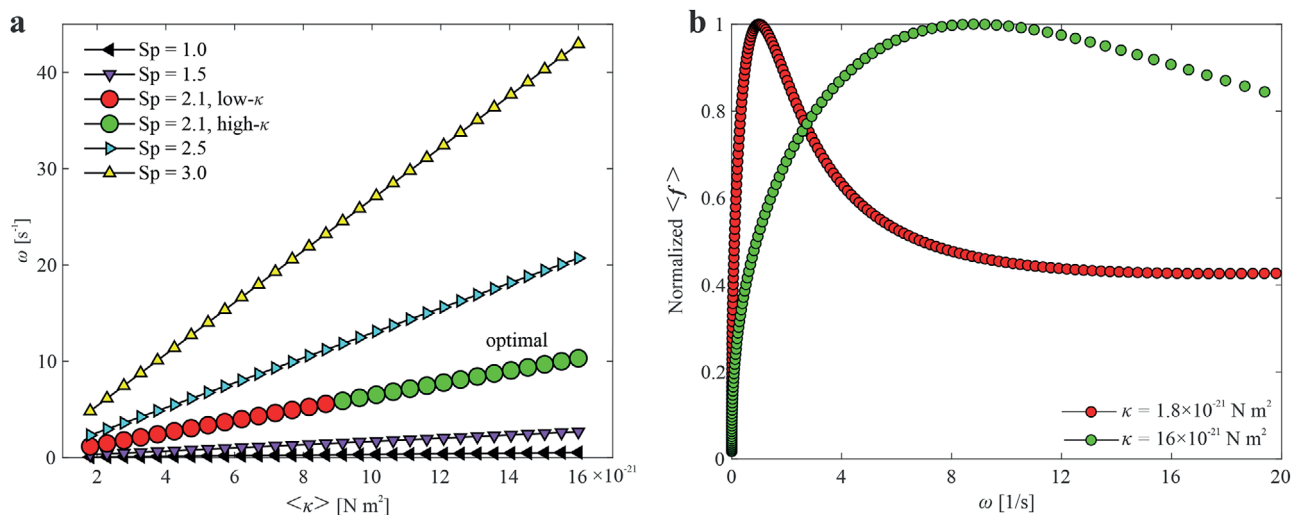
Finally, when the flagellum is coated at the midpiece and principal piece ($m = p = 1$ and $d = 0$) the three observation points along the flagellum restore their original locations at decay rates of 6.71, 6.68, and 6.59 s^{-1}, as shown in Figure 6i–l. Again, we observe that the observation points near the magnetizable cellular segments have faster response than any uncoated cellular segment (distal end). Note also that coating of the midpiece and principal piece allows all points along the length to restore their locations at similar decay rate of 6.66 s^{-1} on average. Therefore, the corresponding bending stiffness is $\langle\kappa(1, 1, 0)\rangle = 8.29 \times 10^{-21}$ N m^2 using Equation (26), while Equation (28) predicts bending stiffness of $\langle\kappa(1, 1, 0)\rangle = 8.08 \times 10^{-21}$ N m^2 using the parameters of the midpiece- and principal piece-coated flagellum.

The simulation results show how spatially varying properties along the length affect the decay rate of the flagellum to the initial configuration. Consequently, the bending stiffness of the flagellum is directly affected by these varying properties based on Equation (28). Nanoparticle-coated flagella with more magnetized cellular segments present a much greater decay rate to the original configuration after the field is removed, and consequently

have higher bending stiffness. For example, a fully coated flagellum has greater decay rate and bending stiffness than any other nanoparticle-coated flagellum.

3.4. Optimal Actuation Frequency

It is well known that optimal swimming using transverse bending waves along a passive filament requires sperm number of 2.1.[34] In the case of magnetizable passive flagellum, the length imposes a significant limitation in realizing this optimal value. This is not the case with soft synthetic microrobots where the length can be controlled during fabrication to approach Sp = 2.1 for a given actuation frequency and properties of physical surrounding. Actuation frequency is also limited by the step-out frequency, which is limited by the field strength, magnetization, and the geometric and fluidic properties of the filament and medium, respectively. Therefore, the influence of the bending stiffness on the sperm number is an important factor in the realization of optimal flagellar propulsion. We allow the nanoparticles to spatially vary along the length, determine the averaged bending stiffness over the length, and calculate the corresponding actuation frequency for sperm numbers in the range $1 \leq$ Sp ≤ 3. **Figure 7** shows that for a given Sp, the actuation frequency is directly proportional to the averaged bending stiffness. For Sp = 2.1, a desirable actuation frequency would be proportional to the bending

2100438 (10 of 15)

ADVANCED
SCIENCE NEWS

www.advancedsciencenews.com

ADVANCED
THEORY AND
SIMULATIONS

www.advtheorysimul.com

Figure 7. Actuation frequency, ω, of a magnetizable segment is calculated for different bending stiffness, κ, and sperm number, Sp, using Equation (1). a) For optimal flagellar propulsion (Sp = 2.1),[34] the optimal actuation frequency is directly proportional to the averaged bending stiffness over the length. b) Optimal propulsive time-averaged thrust force, $\langle f \rangle$,[37] of a flagellum with greater bending stiffness is achieved at higher actuation frequency. Improvement of the frequency response is achieved for flagellum with greater bending stiffness.

stiffness of the flagellum. For example, the actuation of two passive flagella with bending stiffness of 2×10^{-21} and 16×10^{-21} N m^2 at 1.1 and 10.3 rad s^{-1}, respectively, yields Sp = 2.1.

Figure 7a also suggests that the filament can be made relatively flexible and actuated at low frequencies to generate maximum propulsive thrust (see Experimental Section). The filament can also be made stiff but its optimal actuation frequency must be relatively high. This relationship is particularly useful as the length of the flagellum is constant or when considering a geometric constraint on the length of a synthetic filament. The propulsive thrust also shows how the bending stiffness and actuation frequency influence propulsion, as shown in Figure 7b. The propulsive thrust, f, is calculated using the resistive-force theory by applying rotating magnetic field about the axis $\mathbf{e}_1$ for nanoparticle-coated flagella with range of actuation frequency between 0 and 20 Hz and for two representative bending stiffness of 1.8×10^{-21} and 16×10^{-21} N m^2. Associated with the increase in the bending stiffness of the flagellum is an increase in the optimal actuation frequency and overall enhancement in the frequency response. Note that the results in Figure 7a,b are in agreement in that both suggest low-frequency and high-frequency for flagellum with low and high stiffness, respectively.
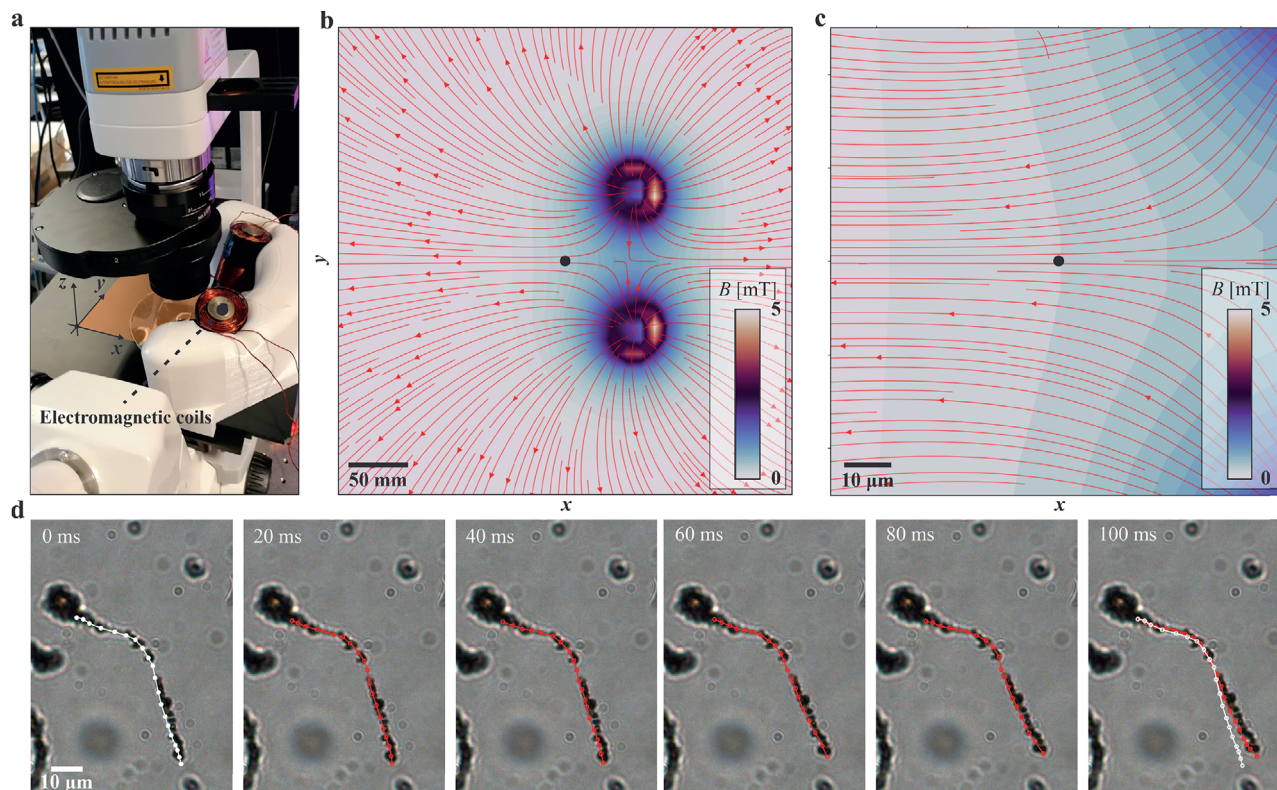
4. Estimation of the Bending Stiffness

Nanoparticle-coated sperm cells are allowed to precipitate on a slide and the various types are observed using a microscope and camera feedback. To characterize the bending stiffness, we often exert a magnetic torque on several cells within a relatively large field-of-view to select the cells that are fixed at the proximal end. Once they are observed, the microscope is focused on one of the cells within a circular field-of-view of ≈ 350 μm in diameter. Two electromagnetic coils are arranged at an oblique angle with respect to the x–y plane that contains the cells, as shown in **Figure 8**a. The coils have angles of 70° and 20° with respect to

the x–y and x–z planes, respectively. The superimposed field of the two coils at the location (small black circle) of the sample is 5 mT (Figure 8b,c). When a nanoparticle-coated cell in a viscous fluid is subject to this magnetic field, the magnetic torque tends to align the flagellum along the magnetic field lines. The amplitude of the deformation of the flagellum is highly dependent on the applied magnetic field and the angle between the magnetic field and the long axis of the cell. Therefore, the magnetic excitation is conducted at three angles (5°, 10°, and 15°) between the long axis of the cell $\mathbf{e}_1$ and the resultant magnetic field. The nanoparticle-coated flagella tend to return to their equilibrium state when the applied field is removed, as shown in Figure 8d. The process is then repeated ten times for each angle and for each group of nanoparticle-coated cells. During each trial, the decay rate is measured, and then the apparent bending stiffness is calculated using Equation (26).

Figure 8d shows a fully coated flagellum immersed in water and fixed at its proximal end. At $t = 0$, the magnetic field is set to zero and the decay rate of the distal end is measured as 2.5 s^{-1}. At $t = 0.1$ s, the flagellum restores its initial configuration before the magnetic field. Similarly, **Figure 9** shows the response of a distal-coated and midpiece-coated flagella when the applied magnetic field is removed. The decay rate of these three nanoparticle-coated flagella differs as predicted by the numerical results, which is expected due to the dependence of the averaged bending stiffness on the location and concentration of the nanoparticles.
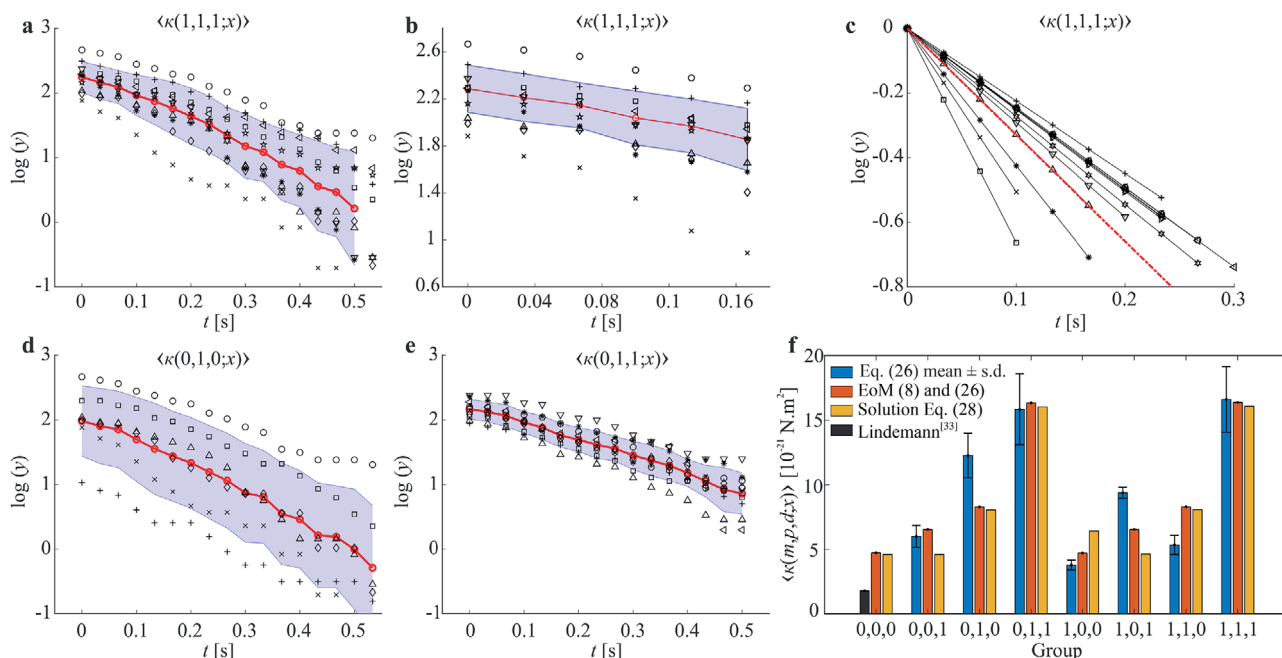
Figure 10a shows the decay rate of a fully coated flagellum for several magnetic excitation and relaxation trials. The decay rate is calculated using the displacement while relaxing toward one-half of the maximum displacement, as shown in Figure 10b. The average decay rate of this fully coated flagellum is -3.3 ± 1.3 s^{-1} ($n = 12$). Using Equation (26), the bending stiffness is $16.61(\pm 2.54) \times 10^{-21}$ N m^2. In contrast, distal- and midpiece-coated flagella restore their original configuration at much slower

Figure 8. The deformation of the flagellum is measured while relaxing toward the equilibrium configuration to determine its bending stiffness. a) Magnetic torque is applied on the magnetizable cells using two electromagnetic coils. b) The magnetic fields of each coil are superimposed and controlled to dynamically excite the flagellum. The axis of each coils has an angle of 70° with the *x*–*y* plane and 20° with the *x*-*z* plane. c) Field strength of 5 mT is applied at the position of the flagellum. d) A sperm cell is surrounded with nanoparticles and is fixed at its head to a solid boundary. At $t = 0$ s, the magnetic field is removed and the energy stored in the flagellum restore its original configuration. The bending stiffness of this sample is designated as $\langle \kappa(1, 1, 1) \rangle$ because all cellular segments are coated with magnetizable nanoparticles. Time-dependent deformations of the passive flagellum are measured after the removal of the magnetic field.
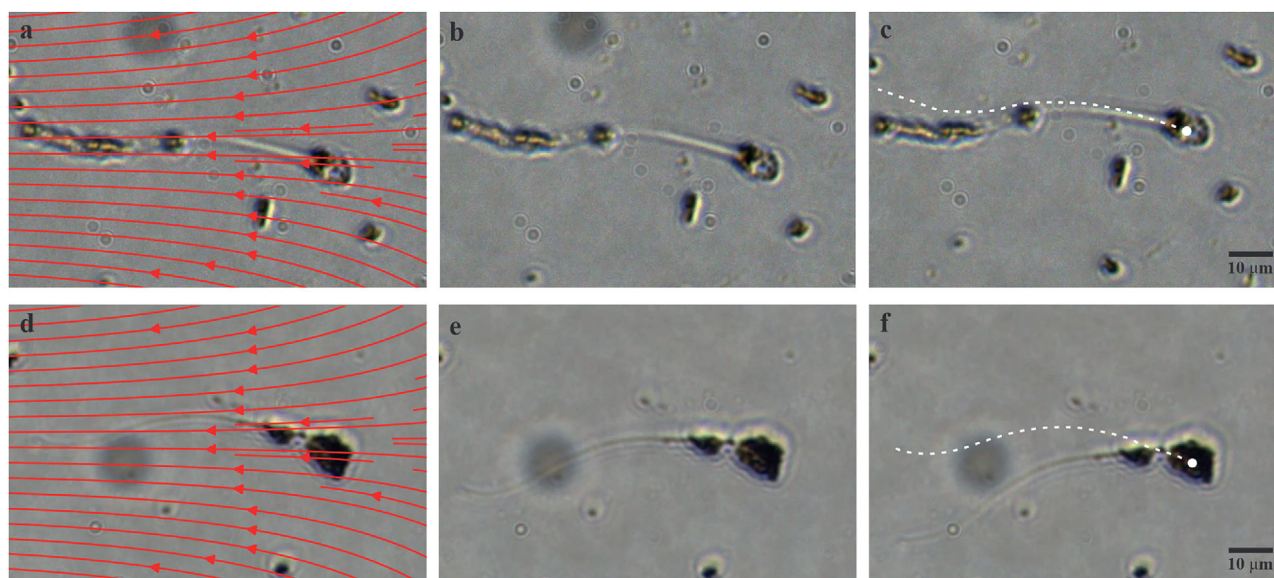
Figure 9. Nanoparticle-coated flagella restore their initial state after the magnetic field with an angle $\angle \mathbf{Be}_1 = 15°$ is removed. The white dashed lines represent the initial configuration of the flagellum. a–c) Distal-coated flagellum restores its initial configuration at decay rate of 0.24 s^{-1} and the average bending stiffness is $\langle \kappa(0, 0, 1) \rangle = 10.86 \times 10^{-21}$ N m^2. d–f) Midpiece-coated flagellum restores its initial configuration at decay rate of 1.419 s^{-1} and $\langle \kappa(1, 0, 0) \rangle = 20.53 \times 10^{-21}$ N m^2.

**ADVANCED
SCIENCE NEWS**

www.advancedsciencenews.com

**ADVANCED
THEORY AND
SIMULATIONS**

www.advtheorysimul.com

Figure 10. The nanoparticle-coated flagellum is driven by magnetic field and its relaxation is measured to determine the bending stiffness. The field is removed ($t = 0$) and the position of its distal end is measured for various coated cellular segments. The average bending stiffness is determined from ten different dynamic excitations using the same cell. a–c) The decay rate of a fully coated flagellum is extracted using the displacement while relaxing toward one-half of the maximum displacement. The average decay rate is -3.3 ± 1.3 s^{-1} ($n = 12$) and the average bending stiffness is $2.49(\pm 1.37) \times 10^{-21}$ N m^2. d) Principle piece-coated flagellum with $\langle \kappa(0, 1, 0) \rangle = 15.5(\pm 1.87) \times 10^{-21}$ N m^2. e) Principle piece and distal-coated flagellum with $\langle \kappa(0, 1, 0) \rangle = 15.8(\pm 2.68) \times 10^{-21}$ N m^2. f) Measured bending stiffness from measured decay rate using Equation (26), simulated response using Equations (8) and (26), and calculated bending stiffness using Equation (28).

Table 1. Relaxation time [s] and average bending stiffness ([N m^2] × 10^{-21}) of the various types of nanoparticle-coated cells. Relaxation time, $\mathcal{T}$, is measured during relaxation of the flagellum and the bending stiffness is calculated using Equation (26). The bending stiffness is proportional to the number of coated cellular segments and the location of the coating along the flagellum.

Cell	Fully uncoated and coated		Single cellular segment			Two cellular segments		
	000	111	001	010	100	011	101	110
$r_m l$	1.875l	1.875l	1.875l	2.2657	1.2089	3.2313	1.0862	1.3127
$\mathcal{T}$	2.0	0.25 ± 0.04	0.49 ± 0.06	0.23 ± 0.01	0.97 ± 0.13	0.15 ± 0.10	0.28 ± 0.01	0.78 ± 0.13
$\langle \kappa \rangle$	1.8[38]	16.61 ± 2.54	6.01 ± 0.85	12.27 ± 1.73	3.79 ± 0.38	15.86 ± 2.74	9.39 ± 0.42	5.34 ± 0.74

rates of 0.24 s^{-1} and 1.419 s^{-1} as shown in Figure 10d,e, respectively. The corresponding average bending stiffness of these cells are $6.01(\pm 0.85) \times 10^{-21}$ and $12.27(\pm 1.73) \times 10^{-21}$.

Figure 10f shows the averaged bending stiffness compared with the numerical results for seven groups of nanoparticle-coated cells. It is evident that the location of the magnetizable nanoparticles has a direct effect on the bending stiffness (**Table 1**). In the case of fully uncoated and fully coated flagella, the averaged bending stiffness is 1.8×10^{-21} and $16.61(\pm 2.54) \times 10^{-21}$ N m^2, respectively. The bending stiffness of a fully coated flagellum is greater than that of uncoated flagellum by eight times or more, which is expected due to the friction between the particles that coat the cell. Figures 1c and 2 show several coated cellular segments with nanoparticles. Sliding friction between these particles is likely to provide a substantial resistance when the magnetic field is applied. Regardless of the location of the coating, the

bending stiffness of the particle-coated cells is greater than that of the uncoated cell, as shown in Figure 10f.

In the case of a single magnetized cellular segment, the averaged bending stiffness is entirely dependent on the location of the cellular segment. The average bending stiffness of midpiece-, principal piece-, and distal-coated flagella are $3.79(\pm 0.38) \times 10^{-21}$, $12.27(1.73) \times 10^{-21}$, and $6.01(\pm 0.85) \times 10^{-21}$ N m^2, respectively. The surface area of the principal piece is much greater than that of the distal end, while the surface area of the distal end is slightly greater than the surface area of the midpiece, leading to the direct relation between the measured bending stiffness and the coated area by the nanoparticles. Similarly, in the case of two magnetized cellular segments, the principal piece- and distal-coated flagellum has a greater bending stiffness ($15.85(\pm 2.74) \times 10^{-21}$ N m^2) than the midpiece- and distal-coated ($9.39(\pm 0.42) \times 10^{-21}$ N m^2) and the

**ADVANCED
SCIENCE NEWS**
www.advancedsciencenews.com

**ADVANCED
THEORY AND
SIMULATIONS**
www.advtheorysimul.com

midpiece- and principal piece-coated $(5.34(\pm 0.74) \times 10^{-21}$ N m$^2)$ flagella.

5. Conclusions

In this work, we present a contactless electromagnetic-based excitation method to estimate the apparent bending stiffness of nanoparticle-coated passive flagella of bull sperm cells. Electrostatic-based self-assembly is used to produce these soft biohybrid systems which possess intrinsic variable stiffness along the length. The method works by dynamically exciting the magnetizable cells using a controlled magnetic field and measuring their relaxation time after the removal of the magnetic field. This method enables us to estimate the bending stiffness of the passive flagella without direct contact and with minimal risk of damage to the samples during characterization. We also develop numerical models to relate the measured relaxation time to the apparent stiffness of the nanoparticle-coated flagella. We show theoretically and experimentally that the bending stiffness is proportional to the location of the magnetized cellular segment with a minimum value of $3.79(\pm 0.37) \times 10^{-21}$ N m^2 for midpiece-coated flagellum, while fully coated flagellum exceeds this by four times.

6. Experimental Section

Electromagnetic System: The dynamic excitation experiments were done using an electromagnetic system and Zeiss Axio Vert.A1 microscope. The electromagnetic system consisted of two orthogonal electromagnetic coils with a tilt angle of 70° with respect to the horizontal x–y plane and 70° with respect to the vertical x–z plane. Each electromagnetic coil (inner diameter 20 mm, outer diameter 40 mm, and length 80 mm) had 3200 turns with a 0.7 mm wire thickness. The maximum superimposed magnetic field at the position of the samples was 5 mT. The samples were prepared and allowed to precipitate on a horizontal slide and it was observe that the head of the cell adheres to the surface, so that the sperm tail can be excited by the magnetic field which led to an elastic deformation of the tail. The dynamic excitation and relaxation of the samples were recorded and the videos were acquired using a camera a (Camera Axiocam 702 mono, Carl Zeiss B.V., Oberkochen, Germany) and a 50× phase objective (Objective LD EC Epiplan-Neofluar 50×/0.55 DIC M27) at 45 frames s^{-1}.

Nanoparticle-Coated Sperm Cells: Nanoparticle-coated cells were prepared using electrostatic-based self-assembly.[20] Bovine sperm from Holstein bulls were obtained from Masterrind GmbH Meißen and stored in liquid nitrogen. The semen straws where thawed in 37 °C water bath for 2 min, before diluting the semen in 1 mL SP-TALP (Caisson labs). The sperm sample was centrifuged at 300 g for 5 min, the supernatant removed and resuspended in distilled water. This washing step was repeated twice before adding the elongated maghemite rice gain-shaped nanoparticles. Samples were stored at 5 °C until further use.

The elastic modulus of the organic body and nanoparticles were $E_s = 1.4$ MPa and $E_p = 22 \times 10^4$ MPa,[39] respectively. Volume of the sperm head was $\frac{4}{3}\pi a b t = 26.2 \times 10^{-18}$ m^3, where $2a = 10$ μm, $2b = 5$ μm, and $2t = 1$ μm are the major diameter, minor diameter, and thickness of the head, respectively. Volume of the midpiece was $\pi (d_f/2)^2 l_m = 1.63 \times 10^{-18}$ m^3. Finally, the volume of the principal piece and distal end was $\frac{1}{3}\pi (l_p + l_d)((d_f/2)^2 + (d_f/2)r + r^2) = 3.85 \times 10^{-18}$ m^3, where r is the diameter of the distal end at $x = l$ (Figure 1), such that $r = d_f(l)/2 = d_f(1 - f)$. Therefore, the total volume of the sperm cell was 31.69×10^{-18} m^3.

Density of the maghemite particles was 4.86 g cm^{-3}. Therefore, the volume of particles of mass of 9×10^{-9} g was 1.85×10^{-15} m^3. The volume of the sperm cell and the nanoparticles yielded an average frac-

tion of $\langle \phi \rangle = V_p/(V_s + V_p) = 0.98$. This volume fraction was much higher than 3.64123×10^{-5} used in simulation and calculation. Reasons could be high concentration at the head, elastic modulus did not follow rule of mixture, particles had smaller effective elastic modulus because they were separated particles.

Numerical Model: Two numerical methods were used to determine the bending stiffness of the nanoparticle-coated flagella. Both methods made use of the equation of motion based on the nominal parameter of the flagella. The first method (dynamic simulation) was dependent on the time-dependent deformation of the flagellum during magnetic excitation and relaxation, whereas the second method (stiffness calculation) directly related the bending stiffness to the nominal parameters of the flagella with the assumption that the taper factor was relatively small.

Dynamics Simulation: The equation of motion (8) was solved for the deformation $\gamma(x, t)$ using a finite difference method based on the nominal parameters of each group (Section 6). Once equipped with a model based on the nominal parameters, Equation (8) was solved numerically and the response of the flagellum during excitation and relaxation was determined (Figures 4–6). The decay rate was determined using $\gamma(x, t)$ and $\gamma(l, t)$ and used to determine the average bending stiffness with Equation (26). This procedure was similar to the experiment in that the decay rate was measured from the response of the flagellum and entered into Equation (26) to determine the average bending stiffness.

Stiffness Calculation: Equation (28) was used to determine the bending stiffness by assuming that the bending stiffness is piece-wise constant along each cellular segment. Similar parameters (ϕ, E_s, and E_p) to those used in the dynamic simulation were used to calculate the elastic modulus and the moment of area using Equations (3) and (6), respectively. Then the constant $r_m(m, p, d)$ of each group was determined (Table 1) and entered into Equation (28) to determine the apparent bending stiffness.

Propulsive Thrust: The propulsive thrust, f, was calculated using

$$\langle f \rangle = \frac{1}{T_c} \int_0^{T_c} \left((\xi_\perp - \xi_\parallel) \int_0^l \frac{\partial \gamma}{\partial t} \frac{\partial \gamma}{\partial x} d\ell \right) dt \tag{31}$$

where T_c is the period of oscillation and the operator $\langle \cdot \rangle$ denotes averaging over the time period, and $\xi_\parallel = 0.5\xi_\perp$ is the tangential drag coefficient. Oscillation of the nanoparticle-coated flagellum was induced by a time-varying magnetic field given by

$$\mathbf{B} = B_0 \left(1 \cos \omega t \ 0 \right) \tag{32}$$

This field magnetized the nanoparticle-coated cellular segments to a magnetization that trails behind $\mathbf{B}$, leading to the deformation γ in the time-averaged force Equation (31).

Conflict of Interest

The authors declare no conflict of interest.

Data Availability Statement

The data that support the findings of this study are available from the corresponding author upon reasonable request.

[1] S. Palagi, P. Fischer, *Nat. Rev. Mater.* **2018**, *3*, 113.
[2] M. Sitti, *Nat. Rev. Mater.* **2018**, *3*, 74.
[3] M. Medina-Sánchez, V. Magdanz, M. Guix, V. M. Fomin, O. G. Schmidt, *Adv. Funct. Mater.* **2018**, *28*, 1707228.
[4] C. Hu, S. Pane, B. Nelson, *Annu. Rev. Control, Rob., Auton. Syst.* **2018**, *1*, 53.
[5] R. Mhanna, F. Qiu, L. Zhang, Y. Ding, K. Sugihara, M. Zenobi-Wong, B. Nelson, *Small* **2014**, *10*, 1953.
[6] F. Qiu, S. Fujita, R. Mhanna, L. Zhang, B. Simona, B. Nelson, *Adv. Funct. Mater.* **2015**, *25*, 1666.
[7] H. Ceylan, I. Ceren Yasa, O. Yasa, A. F. Tabak, J. Giltinan, M. Sitti, *ACS nano* **2019**, *13*, 1666.
[8] P. Erkoc, I. Yasa, H. Ceylan, O. Yasa, Y. Alapan, M. Sitti, *Advanced Therapeutics* **2019**, *2*, 1800064.
[9] H. Xu, M. Medina-Sánchez, V. Magdanz, L. Schwarz, F. Hebenstreit, O. G. Schmidt, *ACS Nano* **2017**, *12*, 327.
[10] L. Kong, J. Guan, M. Pumera, *Curr. Opin. Electrochem.* **2018**, *10*, 174.
[11] Y. Alapan, O. Yasa, B. Yigit, I. C. Yasa, P. Erkoc, M. Sitti, *Annu. Rev. Control, Rob., Auton. Syst.* **2019**, *2*, 205.
[12] L. Sonntag, J. Simmchen, V. Magdanz, *Molecules* **2019**, *24*, 3410.
[13] V. Magdanz, S. Sanchez, O. G. Schmidt, *Adv. Mater.* **2013**, *25*, 6581.
[14] M. B. Akolpoglu, N. O. Dogan, U. Bozuyuk, H. Ceylan, S. Kizilel, M. Sitti, *Adv. Sci.* **2020**, *7*, 2001256.
[15] B.-W. Park, J. Zhuang, O. Yasa, M. Sitti, *ACS Nano* **2017**, *11*, 8910.
[16] S. K. Srivastava, M. Medina-Sánchez, B. Koch, O. G. Schmidt, *Adv. Mater.* **2015**, *28*, 832.
[17] W. Gao, X. Feng, A. Pei, C. R. Kane, R. Tam, C. Hennessy, J. Wang, *Nano Lett.* **2013**, *14*, 305.
[18] X. Yan, Q. Zhou, M. Vincent, Y. Deng, J. Yu, J. Xu, T. Xu, T. Tang, L. Bian, Y.-X. J. Wang, K. Kostarelos, L. Zhang, *Sci. Rob.* **2017**, *2*, eaaq1155.
[19] V. Magdanz, I. S. Khalil, J. Simmchen, G. P. Furtado, S. Mohanty, J. Gebauer, H. Xu, A. Klingner, A. Aziz, M. Medina-Sánchez, et al., *Sci. Adv.* **2020**, *6*, eaba5855.
[20] V. Magdanz, J. Vivaldi, S. Mohanty, A. Klingner, M. Vendittelli, J. Simmchen, S. Misra, I. S. Khalil, *Adv. Sci.* **2021**, *8*, 2004037.
[21] I. S. Khalil, V. Magdanz, J. Simmchen, A. Klingner, S. Misra, *Appl. Phys. Lett.* **2020**, *116*, 063702.
[22] T. Xu, J. Zhang, M. Salehizadeh, O. Onaizah, E. Diller, *Sci. Rob.* **2019**, *4*, eaav4494.
[23] H.-W. Huang, M. S. Sakar, A. J. Petruska, S. Pané, B. J. Nelson, *Nat. Commun.* **2016**, *7*, 12263.
[24] X. Zhao, Y. Kim, *Soft Microbots Programmed by Nanomagnets*, Springer Nature, London **2019**.
[25] T. Wang, Z. Ren, W. Hu, M. Li, M. Sitti, *Sci. Adv.* **2021**, *7*, 19.
[26] B. M. Friedrich, I. H. Riedel-Kruse, J. Howard, F. Jülicher, *J. Exp. Biol.* **2010**, *213*, 1226.
[27] K. König, L. Svaasand, Y. Liu, G. Sonek, P. Patrizio, Y. Tadir, M. W. Berns, B. J. Tromberg, *Cell. Mol. Biol.* **1996**, *42*, 501.
[28] Y. Tadir, W. H. Wright, O. Vafa, T. Ord, R. H. Asch, M. W. Berns, *Fertil. Steril.* **1990**, *53*, 944.
[29] E. Araujo Jr, Y. Tadir, P. Patrizio, T. Ord, S. Silber, M. W. Berns, R. H. Asch, *Fertil. steril.* **1994**, *62*, 585.
[30] Y. Harada, T. Ota, T. Takamatsu, *2007 International Symposium on Micro-NanoMechatronics and Human Science, MHS*, IEEE Piscataway, NJ **2007**, pp. 199–202.
[31] G. Xu, K. S. Wilson, R. J. Okamoto, J.-Y. Shao, S. K. Dutcher, P. V. Bayly, *Biophys. J.* **2016**, *110*, 2759.
[32] D. B. Hill, V. Swaminathan, A. Estes, J. Cribb, E. T. O'Brien, C. W. Davis, R. Superfine, *Biophys. J.* **2010**, *98*, 57.
[33] C. B. Lindemann, W. G. Rudd, R. Rikmenspoel, *Biophys. J.* **1973**, *13*, 437.
[34] E. L. Tony S. Yu, A. E. Hosoi, *Phys. Fluids* **2006**, *18*, 091701.
[35] C. Brennen, H. Winet, *Annu. Rev. Fluid Mech.* **1977**, *9*, 339.
[36] R. Rikmenspoel, *Biophys. J.* **1966**, *6*, 471.
[37] C. H. Wiggins, R. E. Goldstein, *Phys. Rev. Lett.* **1999**, *80*, 3879.
[38] R. Rikmenspoel, *Biophys. J.* **1965**, *5*, 365.
[39] I. Saeki, T. Ohno, D. Seto, O. Sakaia, Y. Sugiyama, T. Sato, A. Yamauchi, K. Kurokawa, M. Takeda, T. Onishi, *Mater. High Temp.* **2011**, *28*, 264.